

*ARMY RESEARCH LABORATORY*



## **Modeling the Radar Signature of Thin Metallic Objects with the AFDTD Software**

**by Jason Cornelius and Traian Dogaru**

**ARL-TR-7063**

**September 2014**

## **NOTICES**

### **Disclaimers**

The findings in this report are not to be construed as an official Department of the Army position unless so designated by other authorized documents.

Citation of manufacturer's or trade names does not constitute an official endorsement or approval of the use thereof.

Destroy this report when it is no longer needed. Do not return it to the originator.

# **Army Research Laboratory**

Adelphi, MD 20783-1138

---

**ARL-TR-7063**

**September 2014**

---

## **Modeling the Radar Signature of Thin Metallic Objects with the AFDTD Software**

**Jason Cornelius and Traian Dogaru**  
**Sensors and Electron Devices Directorate, ARL**

<b>REPORT DOCUMENTATION PAGE</b>				<b>Form Approved OMB No. 0704-0188</b>
<p>Public reporting burden for this collection of information is estimated to average 1 hour per response, including the time for reviewing instructions, searching existing data sources, gathering and maintaining the data needed, and completing and reviewing the collection information. Send comments regarding this burden estimate or any other aspect of this collection of information, including suggestions for reducing the burden, to Department of Defense, Washington Headquarters Services, Directorate for Information Operations and Reports (0704-0188), 1215 Jefferson Davis Highway, Suite 1204, Arlington, VA 22202-4302. Respondents should be aware that notwithstanding any other provision of law, no person shall be subject to any penalty for failing to comply with a collection of information if it does not display a currently valid OMB control number.</p> <p><b>PLEASE DO NOT RETURN YOUR FORM TO THE ABOVE ADDRESS.</b></p>				
1. REPORT DATE (DD-MM-YYYY)	2. REPORT TYPE			3. DATES COVERED (From - To)
September 2014	Final			June–August 2014
<b>4. TITLE AND SUBTITLE</b> Modeling the Radar Signature of Thin Metallic Objects with the AFDTD Software				
<b>5a. CONTRACT NUMBER</b>  <b>5b. GRANT NUMBER</b>  <b>5c. PROGRAM ELEMENT NUMBER</b>				
<b>6. AUTHOR(S)</b> Jason Cornelius and Traian Dogaru				
<b>5d. PROJECT NUMBER</b>  <b>5e. TASK NUMBER</b>  <b>5f. WORK UNIT NUMBER</b>				
<b>7. PERFORMING ORGANIZATION NAME(S) AND ADDRESS(ES)</b> US Army Research Laboratory ATTN: RDRL-SER-U 2800 Powder Mill Road Adelphi, MD 20783-1138				
<b>8. PERFORMING ORGANIZATION REPORT NUMBER</b> ARL-TR-7063				
<b>9. SPONSORING/MONITORING AGENCY NAME(S) AND ADDRESS(ES)</b>				
<b>10. SPONSOR/MONITOR'S ACRONYM(S)</b>  <b>11. SPONSOR/MONITOR'S REPORT NUMBER(S)</b>				
<b>12. DISTRIBUTION/AVAILABILITY STATEMENT</b> Approved for public release; distribution unlimited.				
<b>13. SUPPLEMENTARY NOTES</b>				
<b>14. ABSTRACT</b> In the current AFDTD software implementation, accurate modeling and simulation of scattering from thin metallic objects (such as flat plates) requires a much finer mesh than for non-metallic objects. This is due to the less-than-rigorous implementation of the physical boundary conditions at the interface between the object and the medium. We describe an improvement to the AFDTD algorithm that properly implements the physical boundary conditions at the interface for metallic objects with planar surfaces that lie on the Cartesian coordinate planes. We simulate the far-field scattering caused by a thin metal rectangular plate, as well as a calibration trihedral, run over incident angles between 0° and 90° from 300 MHz to 3 GHz. To demonstrate the faster convergence with respect to cell size, each set of simulations is run with cell sizes of 0.01, 0.005, and 0.0025 m. These results are compared with a Method of Moments solution provided by the FEKO electromagnetic (EM) modeling software to gauge the accuracy of the solution. Through this comparison, we show that while both versions of the AFDTD code can deliver accurate results for non-grazing angles, the newly adapted version does so with a coarser grid over the entire angle range and all polarization combinations.				
<b>15. SUBJECT TERMS</b> computational electromagnetics, finite difference time domain, FDTD, AFDTD, EM				
<b>16. SECURITY CLASSIFICATION OF:</b> A. Report Unclassified		<b>17. LIMITATION OF ABSTRACT</b> UU	<b>18. NUMBER OF PAGES</b> 28	<b>19a. NAME OF RESPONSIBLE PERSON</b> Traian Dogaru
b. ABSTRACT Unclassified				<b>19b. TELEPHONE NUMBER</b> (Include area code) 301-394-1482

Standard Form 298 (Rev. 8/98)  
Prescribed by ANSI Std. Z39.18

---

## Contents

---

<b>List of Figures</b>	<b>iv</b>
<b>Acknowledgments</b>	<b>v</b>
<b>1. Introduction</b>	<b>1</b>
<b>2. Modeling Methodology and Challenges</b>	<b>2</b>
<b>3. Numerical Results</b>	<b>5</b>
3.1 Scattering by a Plate .....	6
3.1.1 Plate Results for V-V Polarization .....	6
3.1.2 Plate Results for H-H Polarization .....	8
3.1.3 Plate Results for V-H Polarization .....	10
3.1.4 Phenomenology of Scattering by a Plate.....	10
3.2 Scattering from a Calibration Trihedral .....	13
3.2.1 Trihedral Results for V-V Polarization .....	13
3.2.2 Trihedral Results for H-H Polarization .....	15
<b>4. Conclusions</b>	<b>16</b>
<b>5. References</b>	<b>18</b>
<b>List of Symbols, Abbreviations, and Acronyms</b>	<b>19</b>
<b>Distribution List</b>	<b>20</b>

---

## List of Figures

---

Fig. 1 FDTD basic Yee cell, centered at coordinates $(i,j,k)$ , where blue arrows represent the locations of the electric field components and red arrows represent the locations of the magnetic field components. The gray-shaded horizontal plane that cuts through the middle of the cell represents the interface between a dielectric and a perfect electric conductor (PEC) medium. ....	2
Fig. 2 Representation of the horizontal electric field components in the AFDTD implementation of a PEC rectangular plate placed in the $x$ - $y$ plane .....	4
Fig. 3 Representation of the simple geometrical shapes (flat rectangular plate and trihedral) employed in the AFDTD software validation of the PEC boundary conditions .....	5
Fig. 4 Simulation setup for flat metal plate validation.....	6
Fig. 5 RCS vs. $\theta$ results for V-V polarization at 1 GHz using the a) old and b) new implementation of the interface boundary conditions for various cell sizes .....	7
Fig. 6 RCS vs. $\theta$ results for V-V polarization at 3 GHz using the a) old and b) new implementation of the interface boundary conditions for various cell sizes .....	8
Fig. 7 RCS vs. $\theta$ results for H-H polarization at 1 GHz using the a) old and b) new implementation of the interface boundary conditions for various cell sizes .....	9
Fig. 8 RCS vs. $\theta$ results for H-H polarization at 3 GHz using the a) old and b) new implementation of the interface boundary conditions for various cell sizes .....	9
Fig. 9 RCS vs. $\theta$ results for V-H polarization at a) 1 GHz and b) 3 GHz for each implementation of the interface boundary conditions .....	10
Fig. 10 Range profiles of the rectangular plates obtained by the AFDTD software using various cell sizes and boundary conditions for a) V-V polarization and b) H-H polarization .....	11
Fig. 11 Analytic RCS calculation compared to the FEKO (reference solution) at a) 1 GHz and b) 3 GHz.....	12
Fig. 12 Simulation setup for the trihedral placed on the ground .....	13
Fig. 13 a) RCS vs. frequency results for a trihedral in free-space for a V-V polarized radar configuration and b) the resulting SAR image produced when using the new boundary condition implementation .....	14
Fig. 14 a) RCS vs. frequency results for a trihedral on a sand-like surface for a V-V polarized radar configuration and b) its resulting SAR image when using the new boundary condition implementation .....	15
Fig. 15 a) RCS vs. frequency results for a trihedral in free-space for a H-H polarized radar configuration and b) the resulting SAR image produced when using the new boundary condition implementation .....	16
Fig. 16 a) RCS vs. frequency results for a trihedral on a sand-like surface for a H-H polarized radar configuration and b) the resulting SAR image produced when using the new boundary condition implementation.....	16

---

## **Acknowledgments**

---

We would like to acknowledge the contributions of Dr Christopher Kenyon and Dr DaHan Liao, both from the US Army Research Laboratory (ARL), for providing the FEKO scattering solution for the calibration trihedral and the rectangular plate, respectively.

**INTENTIONALLY LEFT BLANK.**

---

## 1. Introduction

---

The finite-difference time-domain (FDTD) is one of the major techniques currently used in the numerical modeling of complex electromagnetic (EM) wave problems.<sup>1</sup> Its popularity is justified by the relative simplicity of the original algorithm, combined with the flexibility of the physical scenarios that it can analyze. Significant algorithmic advances over the last two decades, combined with continuous progress in computer hardware architectures, have led to powerful implementations of the FDTD technique, with applications to radar, antennas, communications, optics, metamaterials, etc. The US Army Research Laboratory (ARL) has developed its own FDTD software, named AFDTD (described previously),<sup>2,3</sup> with primary application to radar target signature analysis.

The major issues affecting the accuracy of the FDTD numerical simulations, namely, the material boundary implementation and the numeric dispersion, have been well documented in the literature.<sup>1</sup> In this report, we address the challenge of accounting for the exact boundary conditions on the surface of a metallic object in the FDTD algorithms. The difficulties arise from the fact that only the tangential electric field components are set to zero at this type of boundary, combined with the peculiarities of the basic Yee cell,<sup>1</sup> where the three electric field components are calculated at points slightly staggered in the three-dimensional (3-D) space. Previous versions of the AFDTD software (1.3 and older) set all three electric field components to zero for a Yee cell placed on the boundary, regardless of the spatial orientation of this surface with respect to the Cartesian axes. However, the newer version 1.4 of AFDTD implements more accurate boundary conditions for metallic objects whenever possible, by setting only the tangential electric field components to zero on those surfaces.

Within the AFDTD code framework, this exact boundary condition implementation works only when the object boundary is a planar surface, oriented along one of the principal Cartesian planes ( $x$ - $y$ ,  $x$ - $z$ , or  $y$ - $z$ ). When the boundary surface has any other shape or orientation, the approach described in this report is not possible, due to the nature of the spatial discretization along Cartesian grid lines characteristic to the FDTD algorithm. It should be noted that advanced FDTD techniques have been developed specifically to address the issue of material boundaries non-conformal to the Cartesian axes or principal planes; among them, we should mention the implementation of the FDTD algorithm in non-Cartesian coordinate systems, or use of an unstructured, non-orthogonal grid instead of the basic Yee cell.<sup>1</sup> However, since the AFDTD software implementation is based on the classical Yee algorithm, we limit the exact treatment of the boundary conditions to the scenarios mentioned at the beginning of this paragraph.

In Section 2 of this report, we present a theoretical description of the boundary conditions for the FDTD algorithm, as well as their practical implementation within the AFDTD code. In

Section 3, we offer numerical examples, which include canonical targets, in order to validate the approach. We finish with conclusions in Section 4.

## 2. Modeling Methodology and Challenges

In order to explain the implementation of boundary conditions at the interface between two media, we start with a brief description of the basic FDTD algorithm. The FDTD method is based on discretizing Maxwell's time-domain equations, using finite differences in spatial and temporal dimensions. The computational space, with a uniform, rectangular, grid-like structure, is made of elementary cubic cells. The EM field components are computed along the cell's edges and faces, according to the drawing in Fig. 1, at discrete time steps. Notice that the electric and magnetic field components are staggered with respect to one another, both in time and space. Each cubic cell is assigned the material properties (permittivity, permeability, and conductivity) of the corresponding region in space.

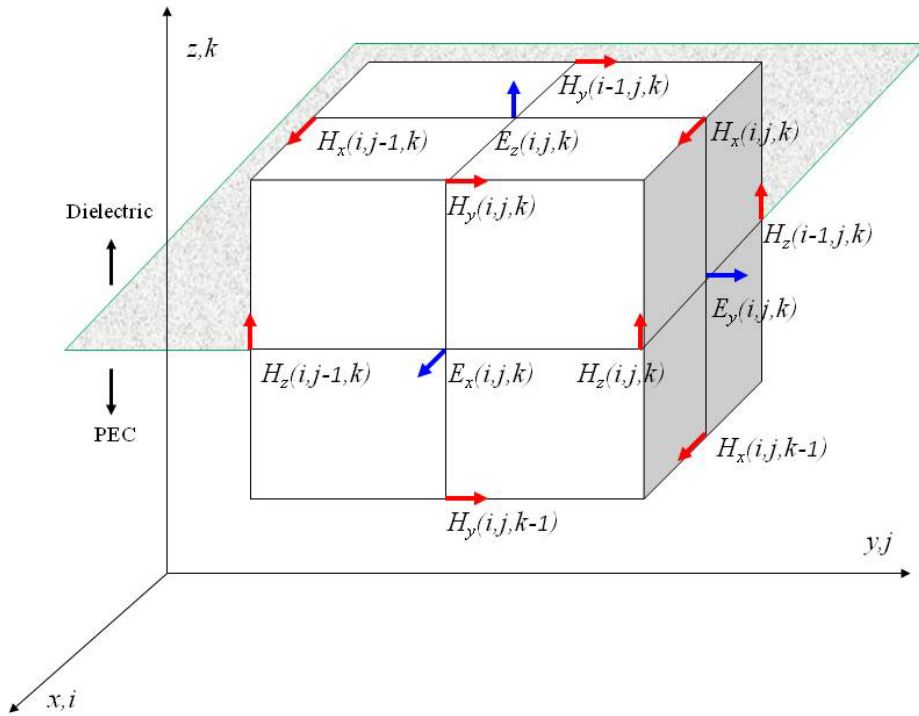


Fig. 1 FDTD basic Yee cell, centered at coordinates  $(i,j,k)$ , where blue arrows represent the locations of the electric field components and red arrows represent the locations of the magnetic field components. The gray-shaded horizontal plane that cuts through the middle of the cell represents the interface between a dielectric and a perfect electric conductor (PEC) medium.

A typical FDTD equation (in this case, the one that updates the  $E_z$  component at cell  $(i, j, k)$  and time step  $n+1$ ) can be written as

$$E_z^{n+1}(i, j, k) = \alpha(i, j, k)E_z^n(i, j, k) + \beta(i, j, k) \left[ \begin{array}{l} H_y^{n+1/2}(i, j, k) - H_y^{n+1/2}(i-1, j, k) - \\ - H_x^{n+1/2}(i, j, k) + H_x^{n+1/2}(i, j-1, k) \end{array} \right], \quad (1)$$

where the factors  $\alpha$  and  $\beta$  depend on the material properties at the cell  $(i, j, k)$ . Thus, for a dielectric material with permittivity  $\epsilon$  and conductivity  $\sigma$ , these factors are

$$\alpha(i, j, k) = \frac{1 - \frac{\sigma(i, j, k)\Delta t}{2\epsilon(i, j, k)}}{1 + \frac{\sigma(i, j, k)\Delta t}{2\epsilon(i, j, k)}} \quad \text{and} \quad \beta(i, j, k) = \frac{\frac{\sigma(i, j, k)\Delta t}{\epsilon(i, j, k)\Delta x}}{1 + \frac{\sigma(i, j, k)\Delta t}{2\epsilon(i, j, k)}}, \quad (2)$$

where  $\Delta x$  and  $\Delta t$  are the cell size and time step, respectively. PEC materials need to be treated in a different way. Since we know that inside a PEC the electric (as well as magnetic) field is zero, we simply set  $\alpha(i, j, k)$  and  $\beta(i, j, k)$  to zero for a cell  $(i, j, k)$  located inside this type of material. This procedure forces both the electric and magnetic field to zero at that cell.

The implementation of the FDTD update equation becomes slightly more complicated when the cell  $(i, j, k)$  is located at the boundary between two media. In the following, we consider the boundary between a PEC and a dielectric material. Basic EM theory shows that,<sup>4</sup> at such an interface, the boundary conditions can be written as

$$\mathbf{n} \times \mathbf{E} = \mathbf{0} \quad \text{and} \quad \mathbf{n} \times \mathbf{H} = \mathbf{J}, \quad (3)$$

where  $\mathbf{n}$  is the surface normal unit vector and  $\mathbf{J}$  is the induced surface current density. While the boundary condition for the tangential magnetic field is implicitly satisfied by the FDTD equations, the electric field counterpart must be enforced explicitly by setting the tangential electric field components to zero, as previously explained. Now assume that the PEC-dielectric interface is parallel to the  $x$ - $y$  plane and cuts through the middle of the Yee cell shown in Fig. 1 (with the PEC below the interface and the dielectric above it). The boundary conditions dictate that we set  $E_x(i, j, k)$  and  $E_y(i, j, k)$  to zero; however, since the  $E_z(i, j, k)$  component is located inside the dielectric medium, it should not be set to zero, but updated according to Eq. 1, with  $\alpha$  and  $\beta$  given by Eq. 2.

In previous AFDTD software implementations (versions 1.3 and earlier), all three electric field components were indiscriminately set to zero for a cell located at a PEC-dielectric interface. Although not always consistent with the exact boundary conditions that follow from Maxwell's equations, this method of treating the interfaces was originally accepted in the AFDTD software due to the simplicity of computer coding. Moreover, extensive software testing did not expose any major errors caused by this procedure. However, as shown in Section 3 of this report, there are particular cases where this method of treating the PEC boundary conditions introduces significant deviations from the correct solution of the EM wave scattering problem.

Version 1.4 of the AFDTD software remedies this issue for PEC boundaries that are planar and parallel to one of the main Cartesian planes ( $x$ - $y$ ,  $y$ - $z$ , or  $x$ - $z$ ). The difference between the two versions is illustrated in Fig. 2, which represents a PEC rectangular plate in the  $x$ - $y$  plane (green contour). All the tangential electric field components ( $E_x$  in red and  $E_y$  in blue) inside the plate contour are set to zero, as dictated by the boundary conditions. However, in the boundary cells, the electric field components normal to those boundaries should not be set to zero, but updated as for the dielectric (background) medium surrounding the plate. These normal boundary components are painted in gray and black in Fig. 2. The gray components are always considered part of the dielectric background (in the old as well as the new implementation). However, the black components are set to zero in the old implementation (version 1.3), whereas the new implementation (version 1.4) considers them part of the background. Additionally, the  $E_z$  components (which are not represented in Fig. 2) are incorrectly set to zero in version 1.3, whereas the implementation in version 1.4 correctly sets them as part of the background.

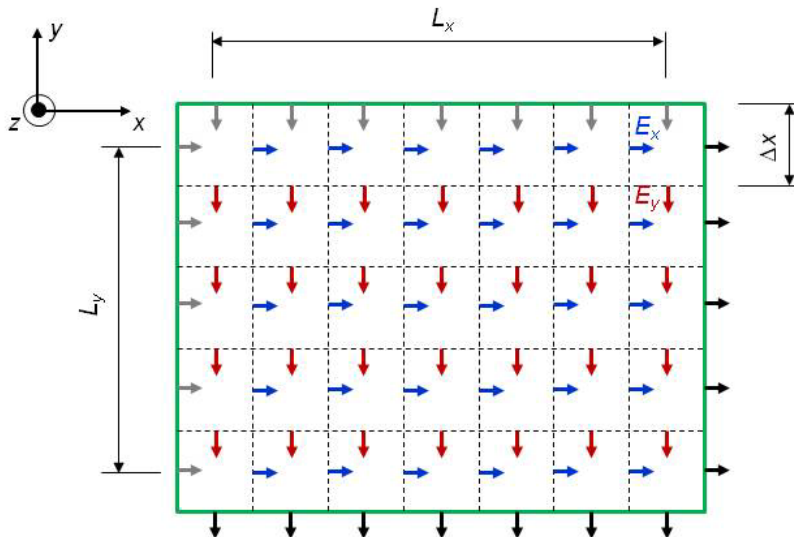


Fig. 2 Representation of the horizontal electric field components in the AFDTD implementation of a PEC rectangular plate placed in the  $x$ - $y$  plane

Although details of the PEC boundary condition implementation in version 1.4 are not included in this report, it should be mentioned that the method only applies to a limited number of geometric objects, which are part of the AFDTDGRID library.<sup>3</sup> These objects are rectangular plate, rectangular box, polygonal plate, prism, disk, circular or elliptical cylinder, ring, and solid ring. Notice that all these objects have at least one planar surface. Additionally, any rotation of the object must ensure that the planar surfaces end up parallel to one of the main Cartesian planes. Particular care is taken to set the correct boundary conditions at the edges formed when two different parts are joined together (such as the trihedral described in Section 3.2).

As expected, there are several limitations to this method of implementing the boundary conditions at the interface of two media in AFDTD. Most importantly, the method only applies

to PEC materials—not to interfaces between two dielectric media. Additionally, the technique is not applied to non-planar (curved) PEC boundaries or planar boundaries that are tilted with respect to the main Cartesian planes; for all these cases, the old-style PEC boundary conditions are employed, where all three electric field components are set to zero. These cases include all the other AFDTDGRID library objects not listed above, as well as any objects obtained by conversion from other mesh formats (such as .facet or .stl files).

In order to validate the new PEC boundary conditions and compare them with the old implementation, we performed a number of simulations describing the EM scattering from two simple shapes: a rectangular plate and a trihedral (Fig. 3). The reason for considering such simple shapes is twofold: 1) scattering from these particular, idealized shapes is very sensitive to model errors, especially at certain angles of incidence/scattering—therefore, small errors in the implementation of the boundary conditions may produce larger radar cross section (RCS) errors than in the analysis of objects with complex shapes; and 2) validating the software for these simple cases (where a reference solution is readily available) gives us confidence to use it in more complex scenarios (where we cannot rely on an independent validation of the results).

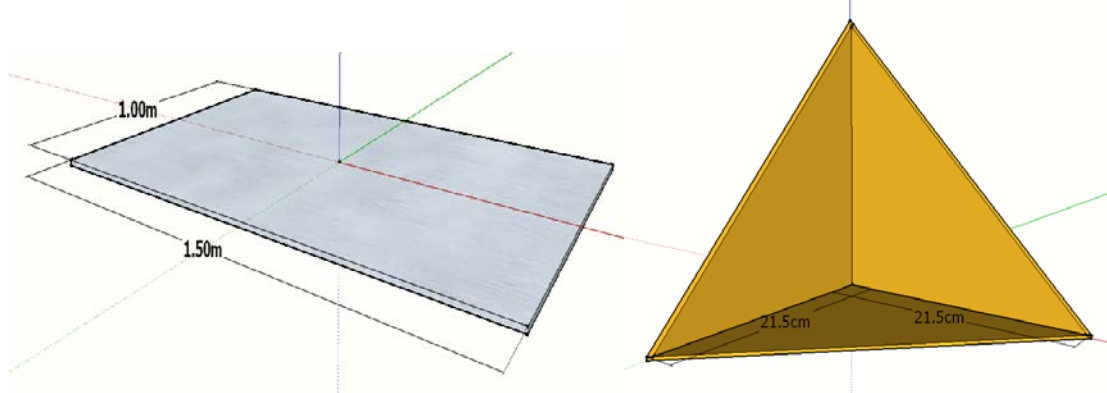


Fig. 3 Representation of the simple geometrical shapes (flat rectangular plate and trihedral) employed in the AFDTD software validation of the PEC boundary conditions

### 3. Numerical Results

We begin this section by briefly describing the parameters common to all simulations. Across all simulations and scenarios described herein, the excitation source and observation points are set up in a monostatic configuration in the far-field. Due to the large bandwidth, we use a 4<sup>th</sup> order Rayleigh pulse<sup>5</sup> for excitation with a center frequency of 1 GHz and a frequency range of 300 MHz to 3 GHz. This setup enables us to simulate a short-pulse, wide-band monostatic radar located far away from the targets of interest. Simulations are conducted for all polarization configurations of the transmitter/receiver pair (i.e., vertical-vertical [V-V], horizontal-horizontal [H-H], vertical-horizontal [V-H], and horizontal-vertical [H-V]). The elevation angle is

measured from the  $z$  axis (denoted by  $\theta$ ), and the azimuth angle (denoted by  $\phi$ ) and the cell sizes are scenario-dependent. These parameters are discussed in the next sections.

### 3.1 Scattering by a Plate

The first scenario we model is the scattering produced by an infinitely thin plate of dimensions 1.5 m by 1.0 m, located in free-space. The plate is placed in the center of the  $x$ - $y$  plane as shown in Fig. 4.

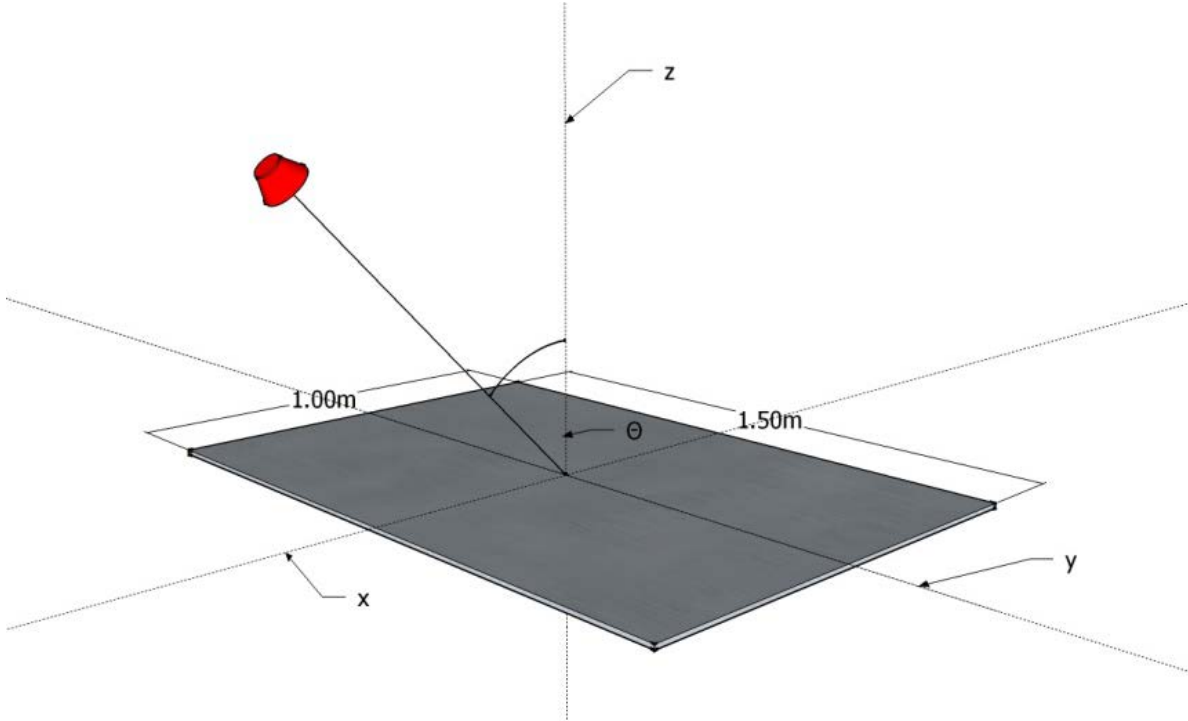


Fig. 4 Simulation setup for flat metal plate validation

For all simulations the radar is oriented in the far-field at  $\phi = 0^\circ$ . The simulation is run over elevation angles that vary from  $0^\circ$  to  $90^\circ$  in  $1^\circ$  increments. Due to the symmetry of the plate, this is sufficient for obtaining results for elevation angles of  $0^\circ$  to  $180^\circ$  within the incidence ( $x$ - $z$ ) plane. Each simulation is repeated using cell sizes of 2.5, 5, and 10 mm. With respect to the largest frequency (3 GHz), these cell sizes correspond to 40, 20, and 10 samples per wavelength, respectively. Results are collected in the frequency domain (versus  $\theta$ ) and compared against a reference solution provided by FEKO,<sup>6</sup> a well-established software for EM modeling, which uses the method of moments (MoM). Time-domain results are featured in Section 3.1.4, where the range profiles and scattering phenomenology of the metal plate are considered. We now proceed with a comparative analysis of the obtained results.

#### 3.1.1 Plate Results for V-V Polarization

Figure 5 shows the RCS of the metal plate for V-V polarization at 1 GHz using both boundary condition implementations. Regarding the old implementation, shown in Fig. 5a, it is clear that

the 10-mm solution begins to deviate significantly (with errors exceeding 5 dBsm) from the FEKO solution at angles from  $50^\circ$  to grazing ( $90^\circ$ ). The 5- and 2.5-mm solutions appear to provide reasonably accurate results (less than 4-dBsm errors) for angles ranging from perpendicular to very close to grazing. However, the 5- and 2.5-mm solutions are inconsistent with the theory at  $90^\circ$  incidence for a vertically polarized wave—for this case, the predicted RCS of the plate is zero (on a linear scale).

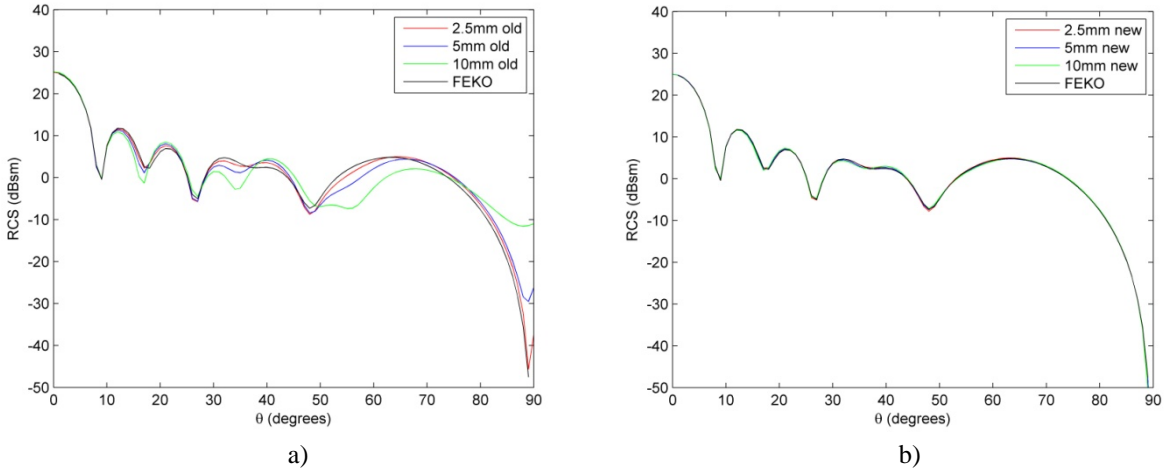


Fig. 5 RCS vs.  $\theta$  results for V-V polarization at 1 GHz using the a) old and b) new implementation of the interface boundary conditions for various cell sizes

On the other hand, Fig. 5b demonstrates that at 1 GHz the newly implemented boundary conditions yield results that are nearly identical to the FEKO solution for all cell sizes. This establishes that, under this scenario, the newly implemented boundary conditions are more accurate and provide a much better convergence rate with respect to cell size when compared to the old implementation. Additionally, Fig. 5b also indicates that at grazing, the new boundary conditions are consistent with the theory predicting zero RCS at these angles.

When comparing the V-V polarization results at 3 GHz (shown in Fig. 6), we first note that, for the same cell size, the spatial sampling rate in the FDTD algorithm is smaller than at 1 GHz, meaning that we expect larger numerical errors at the higher frequency.

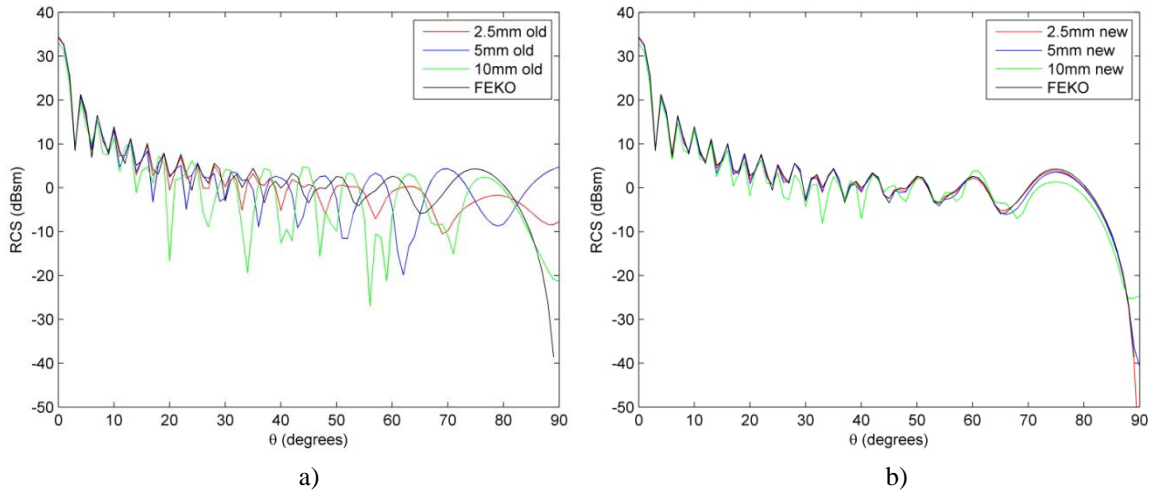


Fig. 6 RCS vs.  $\theta$  results for V-V polarization at 3 GHz using the a) old and b) new implementation of the interface boundary conditions for various cell sizes

For the results shown in Fig. 6a, it is clear that AFDTD is not able to provide reliable results under the old boundary conditions with these cell sizes. This is supported by the fact that with a cell size of 10 mm, errors exceed 15 dBsm, even at a modest angle of  $15^\circ$ . For the smaller cell sizes of 5 and 2.5 mm, the old implementations yield results that deviate from the reference solution by less than 5 dBsm for incident angles below  $45^\circ$ . However, when this angle is exceeded, the deviation becomes larger. In fact, under these conditions, the old implementation does not appear to converge to the reference solution at all. Even with a cell size of 2.5 mm (or 40 samples per wavelength), the old implementation is unable to produce accurate results. Therefore, use of the old implementation would require an even smaller cell size to obtain acceptable results.

Conversely, Fig. 6b illustrates that the new implementation provides results that deviate from the reference solution by no more than 8 dBsm even with the coarsest grid. Increasing the grid resolution to 5 mm produces an even smaller maximum error (no more than 2 dBsm). Using a 2.5-mm cell size yields results that are within a fraction of 1 dBsm to the reference solution over all angles of interest. Additionally, there is clear indication that the new boundary conditions produce a solution set that converges to the reference solution much faster than the old boundary conditions with respect to cell size. Consequently, the new implementation supports the use of coarser grids for the modeling of these types of problems when compared to the old implementation, for the same level of accuracy.

### 3.1.2 Plate Results for H-H Polarization

In examining the results for the H-H polarization at 1 GHz shown in Fig. 7, we note that both implementations of the boundary conditions offer reasonably accurate results at all angles, including those approaching grazing. However, the new implementation creates a better match to the reference solution. Closer inspection of these results reveals that the new implementation

produces maximum errors of 1.2, 0.5, and 0.3 dBsm for decreasing cell sizes over all angles. On the other hand, the old implementation yields slightly larger maximum errors of 3.3, 3.7, and 1.7 dBsm for decreasing cell sizes over the angular range of interest. This offers further evidence that the new implementation is able to provide more accurate results and also allows the use of coarser grids.

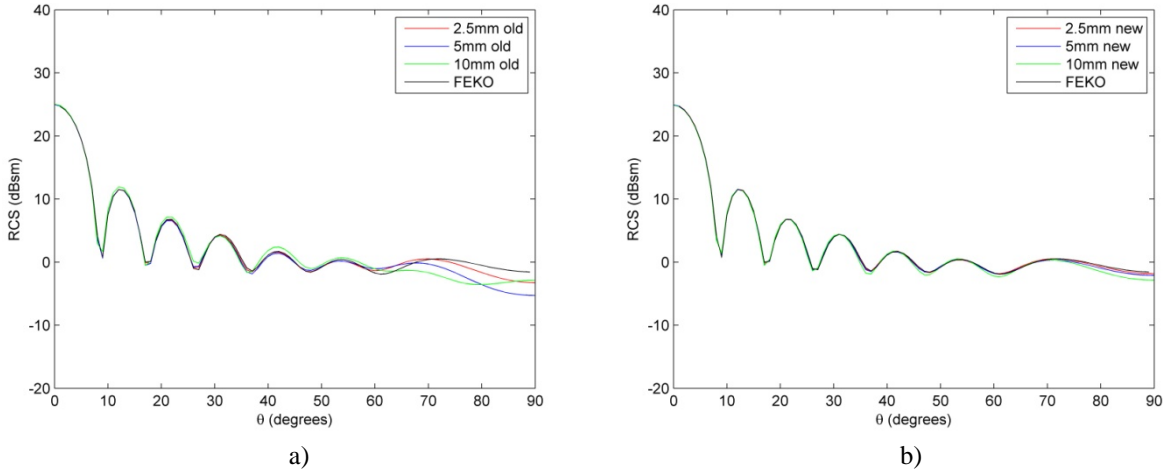


Fig. 7 RCS vs.  $\theta$  results for H-H polarization at 1 GHz using the a) old and b) new implementation of the interface boundary conditions for various cell sizes

Figure 8 shows that at 3 GHz, both implementations yield results that are error-ridden when using a 10-mm cell size. For this cell size, the maximum error of the old implementation is 16.2 dBsm, which occurs at approximately  $48^\circ$  from perpendicular. For the new implementation, this maximum error value is 9.2 dBsm and occurs at roughly  $50^\circ$ . Consequently, in both cases, we must consider a smaller cell size in order to obtain an accurate solution.

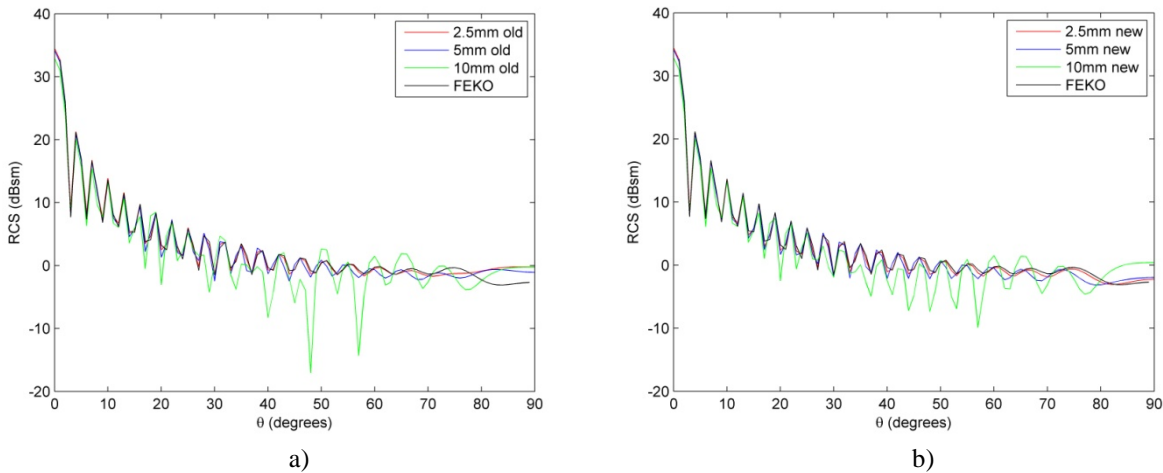


Fig. 8 RCS vs.  $\theta$  results for H-H polarization at 3 GHz using the a) old and b) new implementation of the interface boundary conditions for various cell sizes

When using a cell size of 2.5 or 5 mm, both boundary condition implementations are able to provide more accurate results. For the old implementation, the maximum absolute errors are 2.4 and 2.7 dBsm for 5- and 2.5-mm cell sizes, respectively. For the new implementation, these errors are 1.8 and 0.8 dBsm, respectively. The values of these error figures provide a clear indication that the new implementation is more accurate than the old, while the error trend with respect to cell size offers clear evidence that the new implementation exhibits better convergence than the old one.

### 3.1.3 Plate Results for V-H Polarization

Lastly, we consider the simulation results for a V-H radar configuration (shown in Fig. 9). Due to the symmetry of the metal plate about the incident plane, EM theory predicts that the RCS response seen by a cross-polarization-configured radar is zero (on a linear scale).

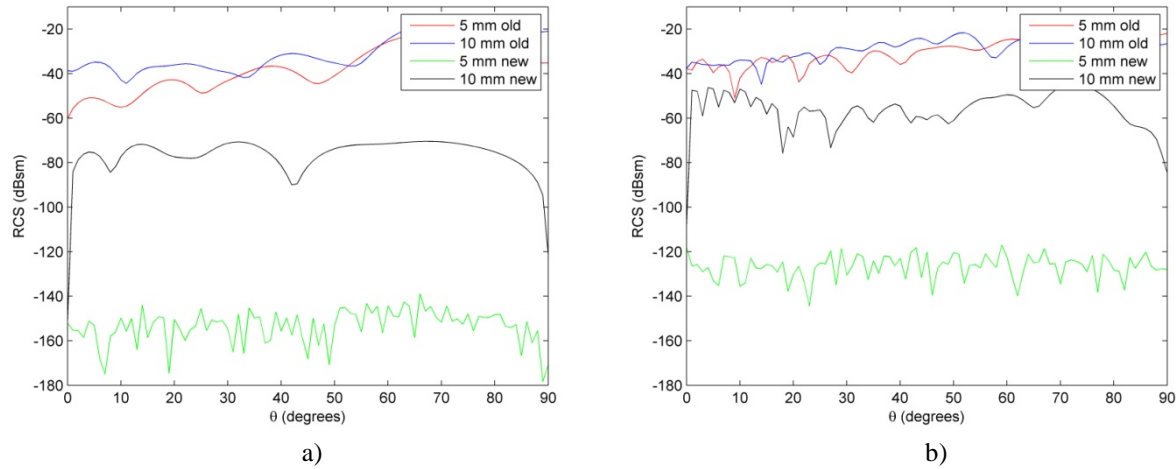


Fig. 9 RCS vs.  $\theta$  results for V-H polarization at a) 1 GHz and b) 3 GHz for each implementation of the interface boundary conditions

Figure 9 demonstrates that the new implementation is in better agreement with this theory in both the 1- and 3-GHz cases. The fact that the new implementation provides a solution at the numerical noise floor level (below  $-100$  dB) is a good indicator that the new implementation of the boundary conditions is behaving correctly in this scenario. The much higher RCS for the old implementation speaks to the numerical errors associated with less-than-rigorous nature of the old boundary conditions.

### 3.1.4 Phenomenology of Scattering by a Plate

Some interesting aspects of the scattering phenomenology from a metallic plate can be evidenced by plotting the range profiles obtained from the backscatter return over the entire bandwidth of the FDTD simulation (Fig. 10). The large bandwidth (which extends from about 0.5 to 2.0 GHz at the 6-dB points) allows the separation of the major scattering centers and mechanisms in the range profiles. The plots in Fig. 10 clearly show the peaks created by diffraction from the leading

edge (LE) and trailing edge (TE) of the plate. Additionally, for V-V polarization, we notice several late-time peaks, which can be explained by multiple (double and triple) diffraction phenomena. Since the multiple diffractions from the plate's edges involve waves propagating along the metallic surface, these phenomena are only supported by vertically polarized fields (for horizontally polarized waves, the tangential-to-the-plate electric field cancels out, so surface waves cannot exist in this polarization). In reality, multiple diffractions occur for H-H polarization as well, but these can only be explained by taking into account higher-order diffraction phenomena.<sup>4</sup>

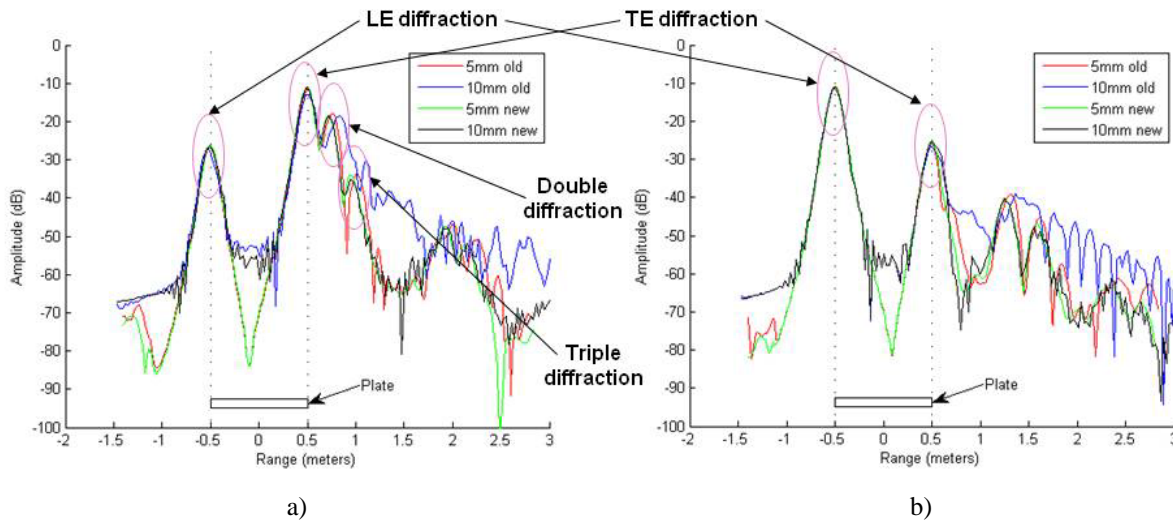


Fig. 10 Range profiles of the rectangular plates obtained by the AFDTD software using various cell sizes and boundary conditions for a) V-V polarization and b) H-H polarization

A rigorous analytic solution to this (apparently simple) scattering problem is, in fact, very complicated. Attempts in this direction were based on Keller's Geometric Theory of Diffraction (GTD),<sup>7</sup> which, in turn, started with the classic Sommerfeld solution to scattering from an infinite (two-dimensional) metallic half-plane.<sup>8</sup> A GTD analysis of the rectangular plate RCS was performed by Ross,<sup>9</sup> with a solution including multiple diffraction terms for each polarization. This solution produces satisfactory results up to about  $80^\circ$  incidence, but diverges (goes to infinity) for larger angles.

Without going into too many mathematical details, a few simple observations can be made regarding the GTD solution based on single LE and TE diffraction. First, the single edge diffraction peaks have the same mathematical expressions for V-V and H-H polarization, with the only difference that the LE and TE switch places between the two cases. Thus, for V-V polarization, the LE peak is proportional to  $1 - \sin \theta^{-1}$ , while the TE peak is proportional to  $1 + \sin \theta^{-1}$  (for H-H polarization, the two expressions need to be swapped). For  $\theta = 45^\circ$ , the ratio between the two peaks is 15 dB—this prediction is very well validated by the simulation (see Fig. 10). The consequence is that, if only single diffraction is considered, the V-V and H-H RCS

of the plate should be identical. In fact, this approximation holds fairly well for angles up to about  $40^\circ$ . For larger angles, the multiple diffraction phenomena present for V-V polarization start to have a larger impact and account for the increasing differences between the two polarizations. When one approaches grazing incidence, the multiple diffraction becomes dominant for V-V polarization; at the same time, the TE single diffraction peak tends to merge with the double and triple diffraction peaks. In this regime, the scattering phenomenology is completely different between V-V and H-H polarization.

In Fig. 11 we plot the reference FEKO solution for the plate RCS at 1 and 3 GHz, together with the analytic solution based on single LE and TE diffraction. The latter can be written as<sup>9</sup>

$$\text{RCS} = \frac{b^2}{\pi} \left| \cos(ka \sin \theta) \pm \frac{j \sin(ka \sin \theta)}{\sin \theta} \right|^2, \quad (4)$$

where  $a$  and  $b$  are the plate dimensions in the  $x$  and  $y$  directions, respectively, while  $k = 2\pi f/c$  is the wave number. The plus sign corresponds to V-V polarization, and the minus corresponds to H-H polarization; however, when the absolute value of the expression in Eq. 4 is calculated, there is no difference between the two. As expected, this solution matches the exact (simulated) RCS for both polarizations up to about  $40^\circ$ . After that, the V-V RCS diverges significantly because of the multiple diffraction terms that were not considered in Eq. 4. Remarkably, the H-H RCS solution obtained from Eq. 4 closely matches the simulated results at all angles, including grazing incidence, within errors of less than 2 dB. This is somewhat surprising, given the fact that, in general, the GTD solution is known to fail at angles close to grazing.

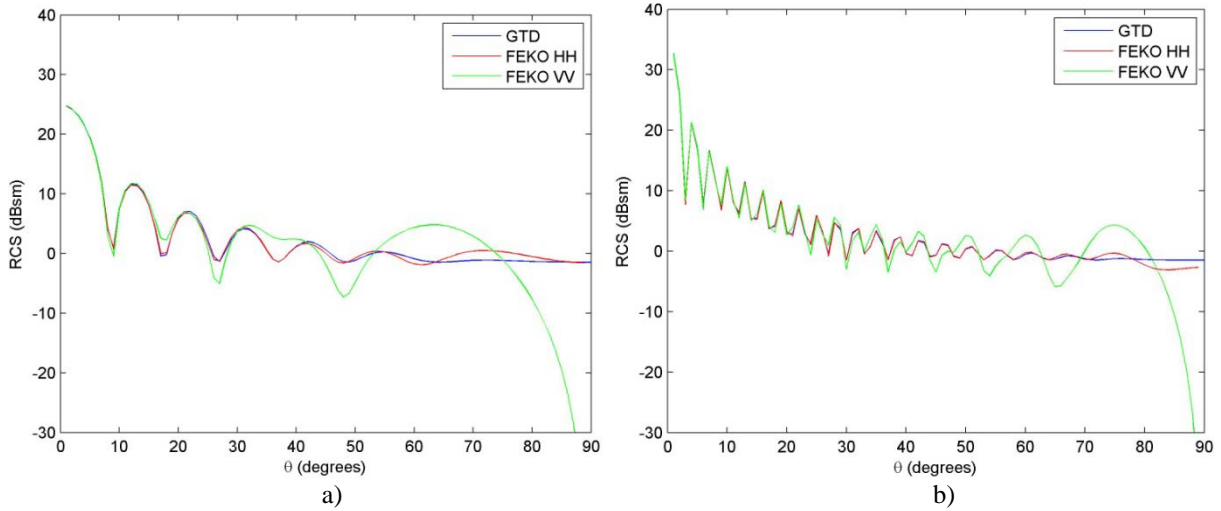


Fig. 11 Analytic RCS calculation compared to the FEKO (reference solution) at a) 1 GHz and b) 3 GHz

Note: The analytic solution is based on GTD using the single diffraction terms.

### 3.2 Scattering from a Calibration Trihedral

The second scenario for which we conduct validation of the new boundary conditions is the scattering produced by a 21.5-cm PEC calibration trihedral. Such trihedrals are typically used to calibrate radar hardware and validate software models. Therefore, the ability to produce accurate modeling results for these targets is crucial. We consider the trihedral in two environments: 1) free-space and 2) placed on a sand-like surface with  $\epsilon_r = 3$  and  $\sigma = 0.0033 \text{ S/m}$ . The latter scenario is depicted in Fig. 12 (with the ground surface shown in green, for contrast).

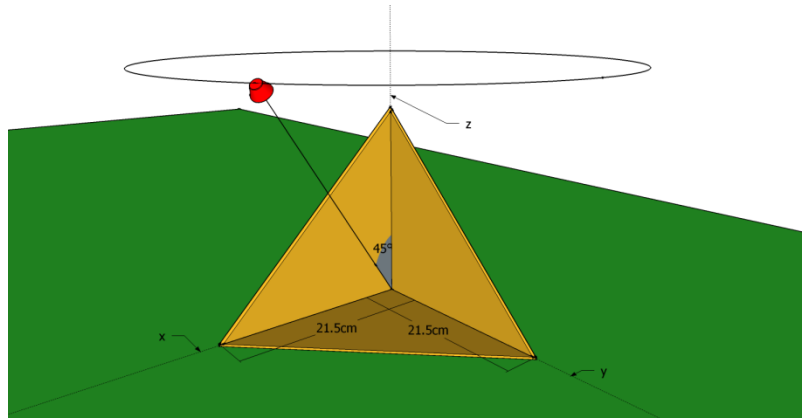


Fig. 12 Simulation setup for the trihedral placed on the ground

To facilitate the creation of synthetic aperture radar (SAR) imagery, we use a fixed elevation angle of  $45^\circ$  while varying the azimuth angle around the clock from  $0^\circ$  to  $360^\circ$  in  $5^\circ$  increments, as shown in Fig. 12. The SAR images are created by a version of the back-projection algorithm<sup>10</sup> that uses all  $360^\circ$  of data. The RCS versus frequency data is examined at  $\theta = 45^\circ$  and  $\phi = 45^\circ$ , where the RCS response is close to the peak.

#### 3.2.1 Trihedral Results for V-V Polarization

We first consider the RCS vs. frequency results (shown in Fig. 13a) for the calibration trihedral placed in free-space for V-V polarization. In comparing the new and old implementations of the boundary conditions under this configuration we note that, for the 300 MHz to 1 GHz range, both methods fall within fractions of a dBsm of the FEKO reference solution. However, from 1 to 3 GHz, the new implementation offers a slight advantage in terms of accuracy. With this in mind, a close examination reveals that the new implementations falls within 0.5 dBsm of the reference solution for all frequencies of interest while the old implementation suffers from a maximum deviation of 1.9 dBsm.

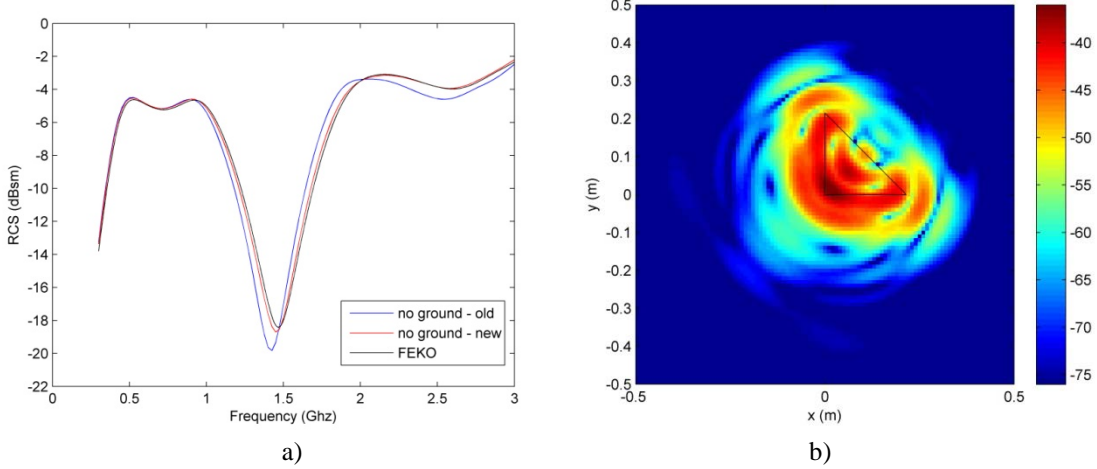


Fig. 13 a) RCS vs. frequency results for a trihedral in free-space for a V-V polarized radar configuration and b) the resulting SAR image produced when using the new boundary condition implementation

Interesting to note is that both implementations, as well as the FEKO solution, exhibit a drastic drop in RCS around 1.5 GHz. While further exploration is needed to explain this phenomenon, it is suspected that this dip can be attributed to the wavelength being near the length of the trihedral edge (0.215 m).

In examining the SAR image (shown in Fig. 13b), which uses the frequency domain results from the new implementation, we observe that the most intense region occurs precisely at the inside corner of the trihedral, as expected. The other corners and trihedral interior, while less intense, are also highlighted in the SAR imagery.

Next we consider the same configuration with an added ground plane. These results are shown in Fig. 14. We immediately note that there is very little difference in the SAR imagery (Fig. 14b) between the scenarios with and without a ground plane. Similarly, with regard to the RCS versus frequency data, we only observe small changes in the overall RCS. For this configuration, the largest deviation we see under the new implementation is 0.7 dBsm, whereas the old implementation is off by maximum of 2.5 dBsm. In both cases, these deviations occur within the deep RCS trough that occurs between 1 to 2 GHz.

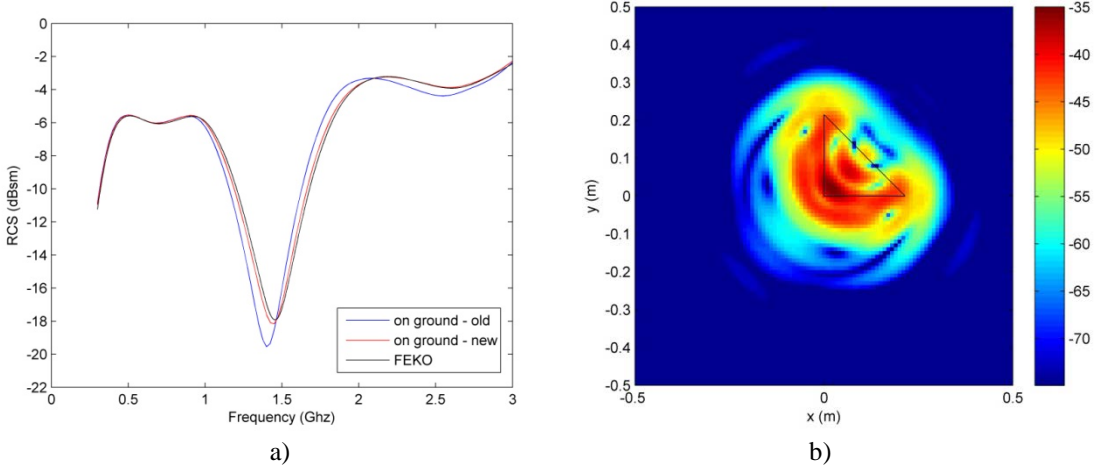


Fig. 14 a) RCS vs. frequency results for a trihedral on a sand-like surface for a V-V polarized radar configuration and b) its resulting SAR image when using the new boundary condition implementation

### 3.2.2 Trihedral Results for H-H Polarization

Lastly, we analyze the trihedral results for both the free-space and ground case for an H-H polarization radar configuration using both boundary condition implementations.

Figure 15 exhibits the results for the case where the trihedral is placed in free-space. Under these conditions, we once again see the improved accuracy of the new boundary conditions. While both solution methods adhere to the FEKO fairly well, the newer implementation does so and achieves the smaller maximum error (0.4 dBsm compared to 1.3 dBsm). To this end, the new boundary conditions are able to provide a more accurate solution under this configuration. When viewing the SAR imagery, we also see the highlighting of the corner, as expected.

Figure 16, on the other hand, shows the H-H results when the trihedral is placed on the ground. We note that, when the trihedral is placed on the ground, the H-H polarization results vary significantly. This is evident when Figs. 15 and 16 are compared. However, like Fig. 15a, Fig. 16a offers more evidence that the new boundary conditions provide a more accurate solution for the calibration trihedral model. This is apparent from the tighter match to the FEKO solution offered by the new implementation.

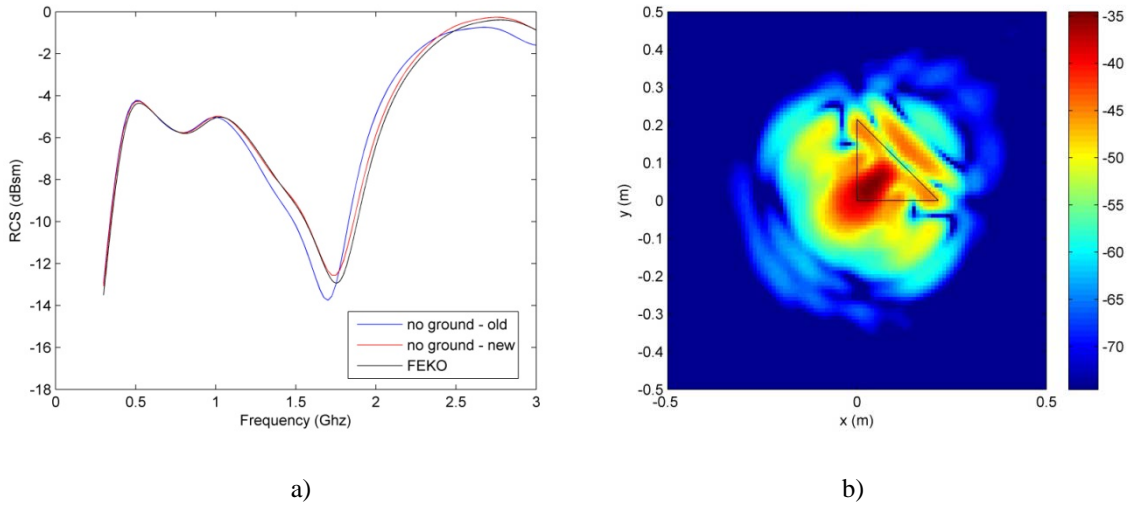


Fig. 15 a) RCS vs. frequency results for a trihedral in free-space for a H-H polarized radar configuration and b) the resulting SAR image produced when using the new boundary condition implementation

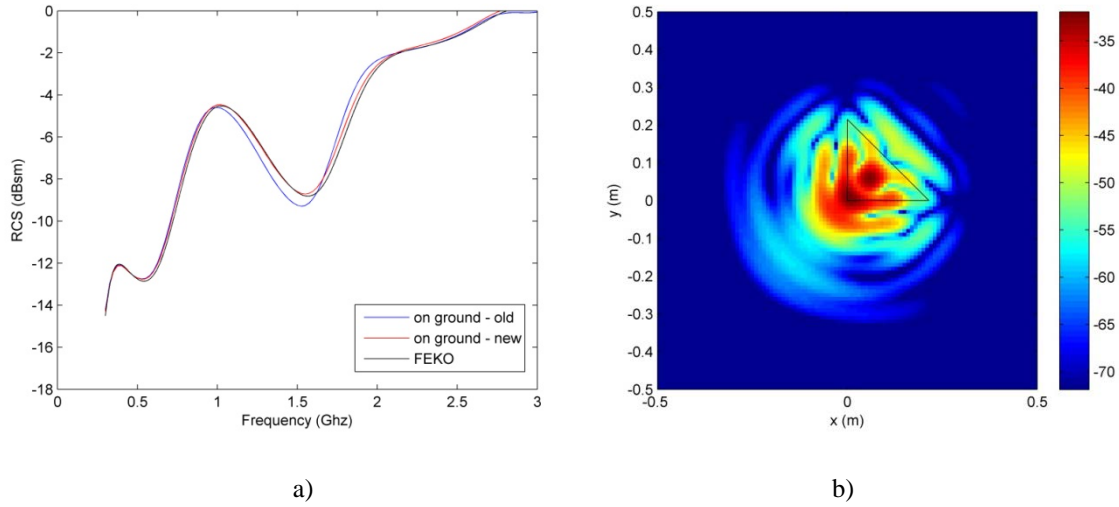


Fig. 16 a) RCS vs. frequency results for a trihedral on a sand-like surface for a H-H polarized radar configuration and b) the resulting SAR image produced when using the new boundary condition implementation

## 4. Conclusions

In modeling radar targets, metallic objects are often represented as PEC materials. In this work, we emphasized the challenges presented by this type of material to the FDTD algorithm. The report contains a brief description of the new PEC interface boundary conditions used by AFDTD, version 1.4, as well as the old conditions used in version 1.3 and earlier. The accuracy of both code versions was tested in EM scattering problems involving canonical objects such as a

rectangular plate (Section 3.1) and a calibration trihedral (Section 3.3). Using the solution provided by the FEKO software as reference, we presented overwhelming evidence that the newer implementation of the boundary conditions found in version 1.4 provides a more accurate solution in all scenarios. Furthermore, in some cases, this increased accuracy can be achieved through the use of a coarser grid. Under these conditions, the new implementation becomes more computationally efficient when compared to the old implementation. This demonstrates the advantages of the new boundary conditions implementation for metallic targets that contain flat surfaces and gives us more confidence in applying the AFDTD software to the simulation of more complex radar scattering scenarios.

---

## 5. References

---

1. Taflove A, Hagness S. Computational electrodynamics: the finite-difference time-domain method, Artech: Norwood, MA, 2000.
2. Dogaru T. AFDTD user's manual. Adelphi (MD): US Army Research Laboratory (US); March 2010. Report No.: ARL-TR-5145.
3. Dogaru T. The AFDTDGRID mesh generation software user's manual. Adelphi (MD): US Army Research Laboratory (US); October 2010. Report No.: ARL-TR-5380.
4. Balanis C. Advanced engineering electromagnetics; Wiley: New York, 1989.
5. Hubral P, Tygel M. Analysis of the rayleigh pulse. Geophysics. 1989;54:654–658.
6. FEKO EM Simulation Software Web page. <http://www.feko.info> (accessed July 2014).
7. Keller JB. Geometrical theory of diffraction. Journal of the Optical Society of America. February 1962;52:116–130.
8. Born M, Wolf E. Principles of optics; Cambridge University Press: Cambridge, UK, 1999.
9. Ross RA. Radar cross section of rectangular flat plates as a function of aspect angles. IEEE Transactions on Antennas and Propagation. May 1966;14:329–335.
10. Soumek, M. Synthetic Aperture radar signal processing; Wiley: New York, 1999.

---

## **List of Symbols, Abbreviations, and Acronyms**

---

3-D	three-dimensional
ARL	US Army Research Laboratory
EM	electromagnetic
FDTD	finite difference time domain
GTD	geometric theory of diffraction
H-H	horizontal-horizontal
H-V	horizontal-vertical
LE	leading edge
MoM	method of moments
PEC	perfect electric conductor
RCS	radar cross section
SAR	synthetic aperture radar
TE	trailing edge
V-H	vertical-horizontal
V-V	vertical-vertical

1 DEFENSE TECH INFO CTR  
(PDF) ATTN DTIC OCA

2 US ARMY RSRCH LABORATORY  
(PDF) ATTN IMAL HRA MAIL & RECORDS MGMT  
ATTN RDRL CIO LL TECHL LIB

1 GOVT PRNTG OFC  
(PDF) ATTN A MALHOTRA

7 US ARMY RSRCH LAB  
(PDF) ATTN RDRL SER U  
JASON CORNELIUS  
TRAIAN DOGARU  
ANDERS SULLIVAN  
KELLY SHERBONDY  
CALVIN LE  
DAHAN LIAO  
CHRISTOPHER KENYON